Rational Direct Synthesis of RbMnFe Nanoparticles (RbMnFe = RbxMn[Fe(CN)6](2+x)/3×nH2O Prussian Blue Analogue)

Thi Thiet Vu, Nathalie Daro, Mathieu Marchivie, Stéphane Mornet, Eric Freysz, Guillaume Chastanet

Rational direct synthesis of RbMnFe nanoparticles (RbMnFe = $Rb_xMn[Fe(CN)_6]_{(2+x)/3}.n.H_2O$ Prussian Blue Analog).

Thi Thiet VU,[1] Nathalie DARO,[1,*] Mathieu MARCHIVIE,[1] Stéphane MORNET,[1] Eric FREYSZ,[2] Guillaume CHASTANET[1,*]

[1] Univ. Bordeaux, CNRS, Bordeaux-INP, ICMCB, UMR 5026, F-33600 Pessac, France.

[2] Univ. Bordeaux, CNRS, UMR 5798, LOMA, F-33405 Talence cedex, France.

Keywords: Prussian Blue Analog, nanoparticles, switching properties

ABSTRACT: In this paper we report the chemical strategy followed to obtain, in a direct way, nanoparticles of the $Rb_xMn[Fe(CN)_6]_{(2+x)/3}.nH_2O$ (RbMnFe) Prussian Blue Analog with the aim of keeping the switching ability of this compound at the nanoscale. The switching property comes from a reversible electron transfer between the iron and manganese ions and depends on the rubidium content in the structure that has to be higher than 0.6. Despite the multifunctionality of this family of compounds and its interest in various applications, no systematic studies were performed to obtain well-defined nanoparticles. This paper relates to such investigation. To draw relationship between size reduction, composition and switching properties, a special attention was brought to the determination of the composition through elemental analysis and structure refinement of powder X-Ray diffraction patterns together with infrared spectroscopy and elemental analysis. Several chemical parameters were explored to control both the size reduction and the composition following a direct synthetic approach. The results show that the smaller the particles, the lower the rubidium content. This observation might prevent the observation of switching properties on very small particles. Despite this antagonist effect, we achieved switchable particles of around 200 nm without any use of surfactant. Moreover, the size reduction is associated to the observation of the electron transfer down to 52% of rubidium in the nanoparticles against 64% in microparticles. This work is of particular interest in processing such nanoparticles into devices.

Introduction

Smart materials sensitive to their environment are being actively developed to cope with the increasing human technological demands. Their properties can react to or be reversibly manipulated by external stimuli. Stimuli as various as mechanical stress, temperature, light, electric or magnetic fields can lead to optical, electric, magnetic, shape, size switches as encountered in piezoelectric materials, shape memory alloys, electro-active polymers, biomaterials, actuators, sensors... Therefore, such materials bear tremendous potential to impact new sustainable systems performances by reducing size, weight, cost and power consumption while improving efficiency, safety, and versatility[1].

Among the numerous switchable systems, metal-to-metal charge transfer (MMCT) assemblies and spin crossover (SCO) molecules are intrinsically multifunctional candidates for devices, as they present a (possibly hysteretic) change between two electronic configurations under external stimuli (temperature, light, pressure, electric field)[2], leading to changes in their optical, electrical, magnetic and mechanical properties. Optical control can be driven in the fs-ns time scale[3], particularly within the hysteresis region[4,5], on nano-sized systems[6a] and even on individual nanoparticles[6b], with very low photoswitching energy[7].

Prussian blue analogs (PBA) are archetypal class II mixed-valence coordination polymers of general formula $C_yA_4[B(CN)_6]_{(8+y)/3}.nH_2O$ (C = alkali cation; y = 0-4; A,B = 3*d* transition metals) envisioned in many applications as magnetic storage and magnetic resonance imaging contrast agent, in electrochromic devices, batteries or catalysis[8,9]. One particular family is standing out from the others as it is intrinsically highly multifunctional. The RbMnFe compound series ($Rb_xMn[Fe(CN)_6]_{(2+x)/3}.nH_2O$, $0 \leq x \leq 1$) can switch between High Temperature (HT, with Mn^{II}-Fe^{III} pairs) and Low Temperature (LT, with Mn^{III}-Fe^{II} pairs) phases, thanks to electron transfer between the Fe and the Mn[10]. This electron transfer is reversible and occurs with a memory effect over a 100 K temperature range, around room temperature[11,12]. Moreover, both LT and HT structures are non-centrosymmetric, leading to non-linear optical properties in both states[13,14] and piezoelectric ferromagnets[15]. Finally, with 97% of Rb^I, a zero-thermal expansion from 15 K to at least 300 K was reported[16]. All these properties strongly depend on the amount of Rb^I inside the structure. For instance, below 60% of Rb^I, the electron transfer is turned off[17].

The $RbMn[Fe(CN)_6]$ compound was first reported in 2002[11] and the phase transition between Mn^{II}(S = 5/2)-NC-Fe^{III}(S = 1/2) in the HT phase and Mn^{III}(S = 2)-NC-Fe^{II}(S = 0) in the LT phase[18] is accompanied by a Jahn-Teller distortion on Mn^{III} [19,20]. As a consequence, there is a structural transition from cubic (HT) to

tetragonal (LT). Many studies have been devoted to the variation of composition from $Rb^{I}Mn^{II}[Fe^{III}(CN)_6].nH_2O$ to $Mn^{II}_{1.5}[Fe^{III}(CN)_6].zH_2O$ by varying the Rb^{I} content between one and zero. It has been shown that the width of the hysteresis loop and the switching temperatures strongly depend on the stoichiometry of the sample[12,21]: the higher the Rb composition, the higher the switching temperatures the narrower the hysteresis. For Rb content lower than 0.61, the charge transfer phase transition is suppressed[17].

All these studies were performed on micro-particles, with the size ranging from 1 µm to 3 µm (Table S1). Particles with sizes lower than 1 µm were reported only three times. In 2006 for 300 nm particles[22], in 2012 for 700 nm particles using PEGM surfactant[16] and in 2013 for a mixture of 50 – 300 nm particles which were employed as sacrificial core to produce hollow Prussian Blue analogue[23]. The very small number of studies at the nanoscale certainly lies on the high solubility of the compound in the aqueous media needed to dissolve the $K_3[Fe(CN)_6]$, RbCl and $MnCl_2$ reactants. This is partially due to the weak stability of the Mn^{II}-NC(-M) bond compared to Co^{II} or Ni^{II} for example that disfavors the nucleation step[9]. Therefore, a subtle balance has to be found to obtain nanoparticles with high Rb^{I} content.

In this paper, we present the synthetic procedures to elaborate switchable rubidium manganese hexacyanoferrate nanoparticles in a rational way. The influence of the concentration of precursors and the reaction time on the size, the composition and the switching properties are experimentally explored and discussed with the aim of establishing a relationship between switching properties and particles size.

Experimental Section

Synthetic protocols

All chemicals were purchased from Sigma-Aldrich and used without purification (purity > 99.99%). The prepared samples were synthesized in water by adding 5 mL of $MnCl_2$ (0.1 M) to 5 mL of a mixed aqueous solution of $K_3[Fe(CN)_6]$ and RbCl, keeping the addition rate at 0.25 mL/min and a vigorous magnetic stirring at 25°C. All the concentrations were calculated using high precision micro-balance and precision glass ware, leading to an error on the concentrations of 1%. All the 12 samples obtained are listed in Table 1.

Impact of $K_3[Fe(CN)_6]$ concentration ([Fe]): The samples were synthesized by slowly adding an aqueous solution (5 mL, 0.1 M) of $MnCl_2$ to a mixed aqueous solution (5 mL) of [Fe] (0.1 M; 0.3 M; 0.5 M; 1.0 M) and RbCl (1 M). After 5 min of stirring, the precipitate was filtered by a Whatman cyclopore polycarbonate membrane 0.4 µm (44 mm in diameter). The powder was washed 5 times directly on top of the polycarbonate membrane by milliQ water to remove the excess of precursors. Then the brown powder was dried in the air at room temperature. Four samples were then obtained: [Fe] = 0.1 M **(1-Fe)**, 0.3 M **(2-Fe)**, 0.5 M **(3-Fe)**, 1.0 M **(4-Fe)**.

Impact of RbCl concentration ([Rb]): the samples were prepared by slowly adding an aqueous solution (5 mL, 0.1 M) of $MnCl_2$ to a mixed aqueous solution (5 mL) of $K_3[Fe(CN)_6]$ (0.3 M or 0.5 M) and RbCl (3 M; 4 M; 5 M). After 5 min of stirring, the same filtration/washing/drying protocol was followed. In addition to **(1-Rb = 2-Fe)** and **(5-Rb = 3-Fe)**, four new samples were then obtained: with [Fe] = 0.3 M, [Rb] = 3 M **(2-Rb)**, 4 M **(3-Rb)** and 5 M **(4-Rb)**; with [Fe] = 0.5 M, [Rb] = 3 M **(6-Rb)**.

Impact of stirring time (t) after addition: the samples were prepared by slowly adding an aqueous solution (5 mL, 0.1 M) of $MnCl_2$ to a mixed aqueous solution (5 mL) of $K_3[Fe(CN)_6]$ (0.3 M) and RbCl (3 M). After addition, the mixed solution was stirred for 1 hour, 24 hours, 48 hours or 60 hours. Then the same filtration/washing/drying protocol was followed. In addition to **(2-Rb)** that was obtained after 5 min of stirring, four new samples were obtained: Stirring time = 1 h **($2\text{-}Rbt_1$)**, 24 h **($2\text{-}Rbt_{24}$)**, 48 h **($2\text{-}Rbt_{48}$)**, 60 h **($2\text{-}Rbt_{60}$)**.

Synthesis of the $Rb_2Mn[Fe(CN)_6].4H_2O$ compound: 5 mL of an aqueous solution of $MnCl_2$ 0.1 M were added (flow rate: 0.25 mL/min) to 5 mL of a mixed aqueous solution of RbCl 1M and $K_4[Fe(CN)_6]$ 0.1 M. After addition, the solution is stirred for 1 hour. The precipitate is filtered and washed with milli-Q H_2O 5-6 times to remove the excess of precursors. After drying in the air the yellow precipitate is obtained. The composition was further estimated as $Rb_2^{II}Mn^{II}[Fe^{II}(CN)_6].4H_2O$ from ICP-OES close to the literature report $Rb_2^{II}Mn^{II}[Fe^{II}(CN)_6].3.5H_2O$[22].

Characterizations

Elemental analyses were performed using ICP-OES (Inductively coupled plasma – optical emission spectrometry) to determine the amount of Rb, Mn and Fe elements. Around 5-7 mg of the compounds were digested in 8 – 10 mL of aqua regia in a HotBlock for 6 – 8 hours at 90°C. Rb element was probed by multiple standard addition method[24]. This method allows an accurate determination of the Rb content by avoiding the complication of the matrix matching effect between the standard and the sample in normal calibration method. Mn and Fe elements were determined by normal calibration curve. C, N elements were analyzed by microanalytical methods. The water content was deduced from: 100% - %Rb - %Mn - %Fe - %C - %N (Table S2). Therefore, the precision on the amount of water is weak.

Powder X-ray diffraction (PXRD) was performed on a PANalytical X'Pert PRO diffractometer (CuKα). The powder samples were transferred in a capillary of 0.4 mm in diameter until the sample height reaches 3 cm. The diffraction patterns obtained were refined by a Rietveld method to extract the composition of the sample and microstructure (Tables S3-S5 and Figures S2-S3).

Infrared Spectroscopy (IR) was performed using a PerkinElmer Frontier FTIR spectrometer. Paraffin was used to stick the powder on the surface of one CaF_2 window. The IR measurements have been done in the transmission mode. The IR spectra inform on the phase and the percentage of $Rb_2Mn[Fe(CN)_6].4H_2O$ impurity, which is a non-switchable compound (Figure S4).

Scanning electron microscopy (SEM) images were obtained using SEM - JEOL JSM 6360A instrument with a 10 kV acceleration voltage and a 16 µA beam current for imaging. The samples were stuck on the carbon tape and metallization was done on top of the samples to increase the conductivity before doing any imaging. The size distribution was fitted using either Gaussian law or logarithmic-normal distribution law which may describe the random nucleation and growth process of these nanoparticles[25] (Figure S5).

Table 1: $Rb_xMn[Fe(CN)_6]_{(2+x)/3}.zH_2O$ compounds

Samples	Formula (ICP-IR)	Formula (XRD)	Size (nm)	$T_{1/2}\downarrow$	$T_{1/2}\uparrow$	ΔT	Imp %
(1-Fe)	$Rb_{0.77}Mn[Fe(CN)_6]_{0.92}.1.3H_2O$	$Rb_{0.71}Mn[Fe(CN)_6]_{0.90}.1.32H_2O$	1665 ± 867	208	286	78	5.0
(2-Fe) = (1-Rb)	$Rb_{0.83}Mn[Fe(CN)_6]_{0.94}.1.0H_2O$	$Rb_{0.82}Mn[Fe(CN)_6]_{0.94}.0.79H_2O$	615 ± 250	209	302	93	4.0
(3-Fe) = (5-Rb)	$Rb_{0.55}Mn[Fe(CN)_6]_{0.85}.3.7H_2O$	$Rb_{0.52}Mn[Fe(CN)_6]_{0.84}.2.15H_2O$	210 ± 55	160	295	135	3.0
(4-Fe)	$Rb_{0.61}Mn[Fe(CN)_6]_{0.87}.3.1H_2O$	$Rb_{0.63}Mn[Fe(CN)_6]_{0.88}.1.60H_2O$	200 ± 64	193	300	107	3.0
(2-Rb)	$Rb_{0.75}Mn[Fe(CN)_6]_{0.92}.0.5H_2O$	$Rb_{0.69}Mn[Fe(CN)_6]_{0.90}.1.48H_2O$	230 ± 76	191	291	100	3.0
(3-Rb)	$Rb_{0.82}Mn[Fe(CN)_6]_{0.94}.0.15H_2O$	$Rb_{0.80}Mn[Fe(CN)_6]_{0.93}.0.93H_2O$	364 ± 189	216	298	82	4.0
(4-Rb)	$Rb_{0.87}Mn[Fe(CN)_6]_{0.96}.0.05H_2O$	$Rb_{0.82}Mn[Fe(CN)_6]_{0.94}.0.82H_2O$	655 ± 373	217	303	86	5.0
(6-Rb)	$Rb_{0.67}Mn[Fe(CN)_6]_{0.89}.3.56H_2O$	$Rb_{0.66}Mn[Fe(CN)_6]_{0.89}.1.57H_2O$	300 ± 150	181	291	110	3.5
(2-Rbt$_1$)	$Rb_{0.82}Mn[Fe(CN)_6]_{0.94}.0.07H_2O$	$Rb_{0.78}Mn[Fe(CN)_6]_{0.93}.1.02H_2O$	287 ± 188	198	297	99	6.0
(2-Rbt$_{24}$)	$Rb_{0.90}Mn[Fe(CN)_6]_{0.96}.0.04H_2O$	$Rb_{0.90}Mn[Fe(CN)_6]_{0.97}.0.53H_2O$	613 ± 283	235	306	71	4.0
(2-Rbt$_{48}$)	$Rb_{0.86}Mn[Fe(CN)_6]_{0.95}.2.4H_2O$	$Rb_{0.83}Mn[Fe(CN)_6]_{0.94}.0.79H_2O$	482 ± 309	218	301	83	4.0
(2-Rbt$_{60}$)	$Rb_{0.89}Mn[Fe(CN)_6]_{0.96}.0.40H_2O$	$Rb_{0.88}Mn[Fe(CN)_6]_{0.96}.0.56H_2O$	454 ± 303	206	306	100	5.6

Magnetic measurements were performed on a Superconducting Quantum Interference Device (SQUID) magnetometer MPMS 5XL with temperature scanning rate of ± 0.5 $K.min^{-1}$ (to prevent thermal quenching of the HT phase) under 5000 Oe of applied magnetic field. Each sample was prepared in a polypropylene bag whose diamagnetic contribution was removed for data treatment. The thermally-induced excited spin-state trapping (TIESST) was first obtained by fast cooling of the sample from room temperature to 10 K within the SQUID cavity. After thermal stabilization at 10 K for few minutes, the temperature was increased at a rate of 0.5 $K.min^{-1}$ until 340 K[26]. Then two cycles from 340 to 10 K were performed. Only the second cycles are presented in this paper (Figure S6).

Ultraviolet-visible (UV-Vis) reflectance spectra were recorded on a Shimadzu UV-3600 spectrometer. $BaSO_4$ white standard DIN 5033 from Merck was used as a reference (Figure S7). These characterizations were systematically performed at room temperature. Only one compound was studied at low temperature to probe the color change.

Results and discussion

Synthetic strategy

Small variations in the synthetic procedures may give rise to materials that differ considerably in composition and physical behavior[27]. Therefore, the usual reaction conditions can be tuned to modulate the particles size. However, we have to keep in mind that Rb^I amount above 60 % is required to obtain switching properties. Among the numerous chemical and physical parameters to explore, we first focused our attention on the reactant concentrations and the reaction times (Figure 1). We therefore varied the concentration of $K_3[Fe(CN)_6]$ and RbCl and the stirring time after mixing the precursors. The prepared materials were synthesized in water by adding 5 mL of $MnCl_2$ (0.1 M) to 5 mL of a mixed aqueous solution of $K_3[Fe(CN)_6]$ and RbCl, keeping the addition rate at 0.25 $mL.min^{-1}$ and a vigorous magnetic stirring at 25 °C. The $K_3[Fe(CN)_6]$ concentration was varied from 0.1 to 1.0 M (green arrow in Figure 1). From the examination of the size and switching properties, the RbCl concentration was then varied from 1.0 M to 5.0 M (blue arrows in Figure 1) starting from the iron concentration of 0.3 M and 0.5 M. Similarly, the stirring time, lasting from 5 min to 60 h (pink arrow in Figure 1), was varied fixing the iron hexacyanoferrate and rubidium chloride concentrations at 0.3 M and 3 M, respectively. On Figure 1 it has to be noticed that compounds **1-Rb** is equivalent to **2-Fe** (as well as **5-Rb** and **3-Fe**). The only difference lies in their code names. We have chosen this sample codification to facilitate the discussion.

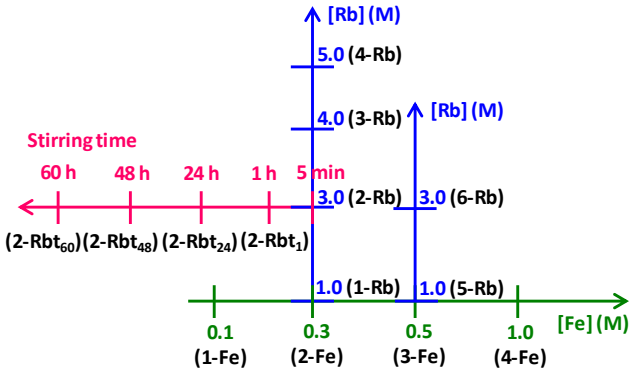

Figure 1: Flow chart showing the synthetic strategy followed to downsize the $Rb_xMn[Fe(CN)_6]_{(2+x)/3}.nH_2O$ particles.

For each sample obtained, a particular attention was brought to the determination of the composition since it is a key parameter for these compounds. Therefore, we used two approaches (ICP-OES and PXRD) to obtain accurate values. Moreover, in these synthesis, some $Rb_2Mn[Fe(CN)_6].4H_2O$ impurities can be observed in which the manganese and the iron are both divalent preventing the electron transfer. Before discussing the effect of the reaction conditions on the size and composition we will first describe in details the determination of the composition.

Composition of the RbMnFe samples

All the samples synthesized were characterized by ICP-OES, using a multiple standard addition method for the Rb element[24]. This method allows to get rid of the overlapping issue of the rubidium signal from the sample and the chlorine signal from

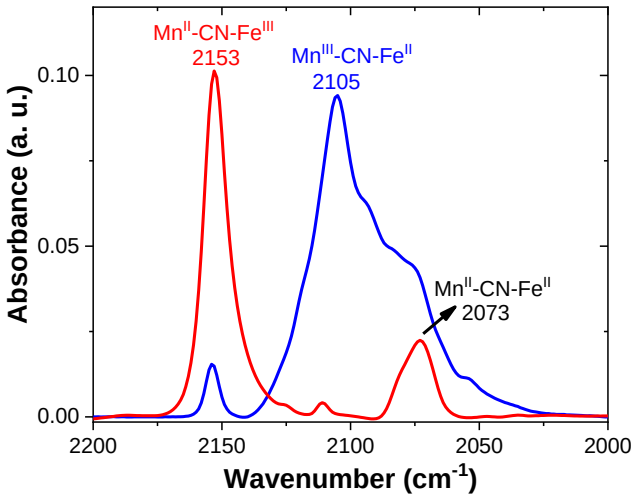

Figure 2: FTIR spectra of **(2-Rbt$_{24}$)** in the HT (red) and 60% LT (blue) phases. (%LT is deduced from Rietveld refinement (Figure S4)).

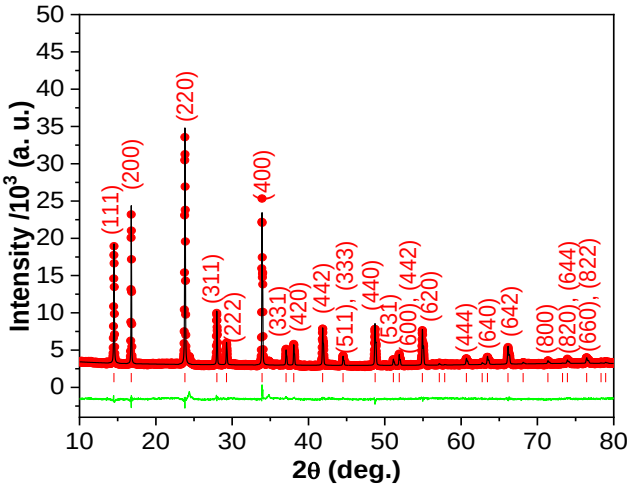

Figure 3: Experimental (●) and simulated (-) PXRD diffractogram recorded at RT of **(2-Rbt$_{24}$)**. The green line stands for the difference between these two XRD patterns and the red bars represent the calculated positions of the Bragg reflections.

the digestion solution. The details of the ICP-OES results are shown in the Table S2. In addition, powder X-ray diffraction was performed on each sample and Rietveld refinement was conducted on each pattern. As reported in the literature, such compound may exhibit some $Rb_2^{I}Mn^{II}[Fe^{II}(CN)_6].4H_2O$ impurities after synthesis whose amount can be determined by infrared spectroscopy.

Indeed, the CN^- stretching frequency is strongly dependent on the oxidation state and the spin state of the metal it bonds. Figure 2 shows the CN^- stretching frequencies in the HT phase at room temperature (RT) and in the LT phase obtained by hanging the powder on top of the liquid nitrogen vapor for 20 min. At RT, a sharp band of Mn^{II}-NC-Fe^{III} is observed at 2153 cm^{-1} typical of the HT phase. Another band is observed at 2073 cm^{-1} and is attributed to Mn^{II}-NC-Fe^{II} species that correspond to the impurity[28] (Figure S1). As the LT phase is induced using liquid nitrogen vapor, the intensity of the HT phase band decreases and a new broad band around 2105 cm^{-1} appears that corresponds to the LT Mn^{III}-NC-Fe^{II} species. There is a fraction of HT phase that still remains at 2153 cm^{-1} in the LT phase spectrum. The ratio of the oscillator strength of the Mn^{II}-NC-Fe^{III} band to that of the Mn^{II}-NC-Fe^{II} band is 0.17[22]. The ratio of the area of the Mn^{II}-NC-Fe^{III} band to that of the Mn^{II}-NC-Fe^{II} band is equal to the ratio of Mn^{II}-NC-Fe^{III} and Mn^{II}-NC-Fe^{II} in the precipitate multiplied by 0.17. From that calculation, the percentage of impurity $Rb_2^{II}Mn^{II}[Fe^{II}(CN)_6].4H_2O$ can be estimated (Figure S4).

As an example, the PXRD pattern of **(2-Rbt$_{24}$)** recorded just after synthesis at room temperature (RT) is shown in Figure 3. The spectrum exhibits the typical features of the HT phase with face-centered cubic structure (F-43m)[28] (Figure S2). Rietveld refinements of the PXRD patterns were performed using the Jana2006 sofware[29]. Red dots, black line, green line and red vertical lines are the observed plot, calculated pattern, their difference, and the Bragg peak positions respectively. The unit cell parameters were refined to a = b = c = 10.563 Å. Miller indices of the reflections were extracted from this unit cell in the F-43m space group and are provided between brackets on Figure 3. From this Rietveld refinement, the composition can be extracted from the ratio of the atomic occupancy of each element in the unit cell. A better accuracy on the composition compared to CHNS-ICP-OES is obtained from the refined atomic occupancies. This is especially true regarding the amount of "structural" water molecules that are all refined (zeolitic and lattice water) while using elemental analysis the precision is weak. This method allows us to obtain the composition directly without taking into account the amount of the impurity from IR

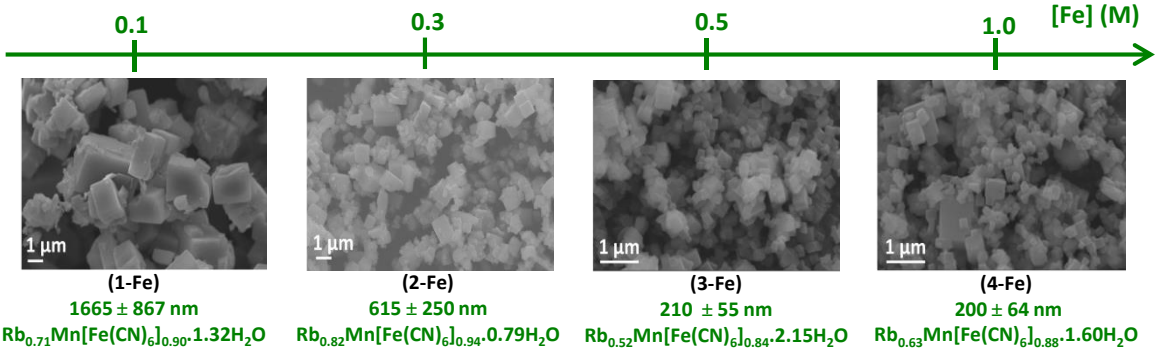

Figure 4: Chart showing the impact of $[K_3[Fe(CN)_6]]$ on the composition and size with the corresponding SEM images of each compound.

spectra, because the diffraction peaks of the impurity do not overlap with that of the compound (Figure S1). The PXRD patterns of the other compounds are presented in Figure S2.

Table 1 gathers information about composition, size and properties for the $Rb_xMn[Fe(CN)_6]_{(2+x)/3}.zH_2O$ compounds illustrated in Figure 1. The formulas, presented in the two first columns, were obtained by different methods: ICP-OES subtracted by the impurity fraction (this value of the percentage deduced from IR spectra appears in the last column) and from Rietveld refinement of the XRD patterns. It is noticeable that the composition deduced from ICP-OES and IR spectroscopy takes into account two errors. More precisely, ICP-OES method shows that the deviation of the measured values are within 0.5 % (absolute) of the expected values[11,30,31]. As PXRD allows to better extract the amount of water molecules for the rest of the study, we use the composition resulting from PXRD. All the discussion is then based on these compositions.

The effect of $K_3[Fe(CN)_6]$ concentration

Figure 4 gathers the information about the size and composition of four different compounds obtained when the $K_3[Fe(CN)_6]$ concentration is increased from 0.1 M to 1.0 M. The SEM images demonstrate that all the compounds have a cubic morphology. In the literature, the morphology of the particle was reported as cubic[31], rectangular[12] or plate-shaped[16] depending on the study. The size distributions of each compound are presented in the figure S5 and give 1665 ± 867 nm **(1-Fe)**, 615 ± 250 nm **(2-Fe)**, 210 ± 55 nm **(3-Fe)** and 200 ± 64 nm **(4-Fe)**. As a consequence, when the concentration of $K_3[Fe(CN)_6]$ increases from 0.1 M to 1.0 M, the size of the particle decreases 8 times from 1.665 µm to 200 nm. This size reduction might come from the excess of $K_3[Fe(CN)_6]$ when the concentration increases that provides negative charges on the surface of the particles leading to electrostatic repulsive forces that favors the particles dispersion and prevent their aggregation and so the formation of bigger particles[9]. When the $K_3[Fe(CN)_6]$ concentration increases, the coherent domain size obtained from PXRD in Table S6 is unchanged from 138 nm to 143 nm, while the size from SEM decreases. It supports that higher $K_3[Fe(CN)_6]$ concentration inhibits the particles' aggregation.

Regarding the composition, and especially the Rb^I content there is no general trend. Indeed, along the series, the Rb^I content evolves as $Rb_{0.71}$ **(1-Fe)**, $Rb_{0.82}$ **(2-Fe)**, $Rb_{0.52}$ **(3-Fe)** and $Rb_{0.63}$ **(4-Fe)**.

Increasing the concentration of the iron precursor above 0.3 M allows the size reduction down to around 200 nm, but the Rb^I content remains relatively low 0.52 and 0.63. To preserve the switching properties, we need the Rb^I content to be higher than 0.6. We therefore studied the effect of RbCl concentration on the size and the composition, starting from **(2-Fe)** and **(3-Fe)**. These compounds are different enough in terms of size and composition to examine the influence of increasing the amount of rubidium in the synthesis.

The effect of [RbCl] concentration

Figure 5 shows the SEM images and the evolution of the size and composition of RbMnFe particles when the [RbCl] increased from 1.0 M to 5.0 M, starting from two different concentrations of the iron precursor. The cubic particles sizes of the samples are 617 ± 250 nm **1-Rb = 2-Fe)**, 230 ± 76 nm **(2-Rb)**, 364 ± 189 nm **(3-Rb)**, 655 ± 373 nm **(4-Rb)**, 210 ± 55 nm **(5-Rb = 3-Fe)**, 300 ± 150 nm **(6-Rb)**. It appears that the higher the RbCl concentration, the bigger the particles size. For instance,

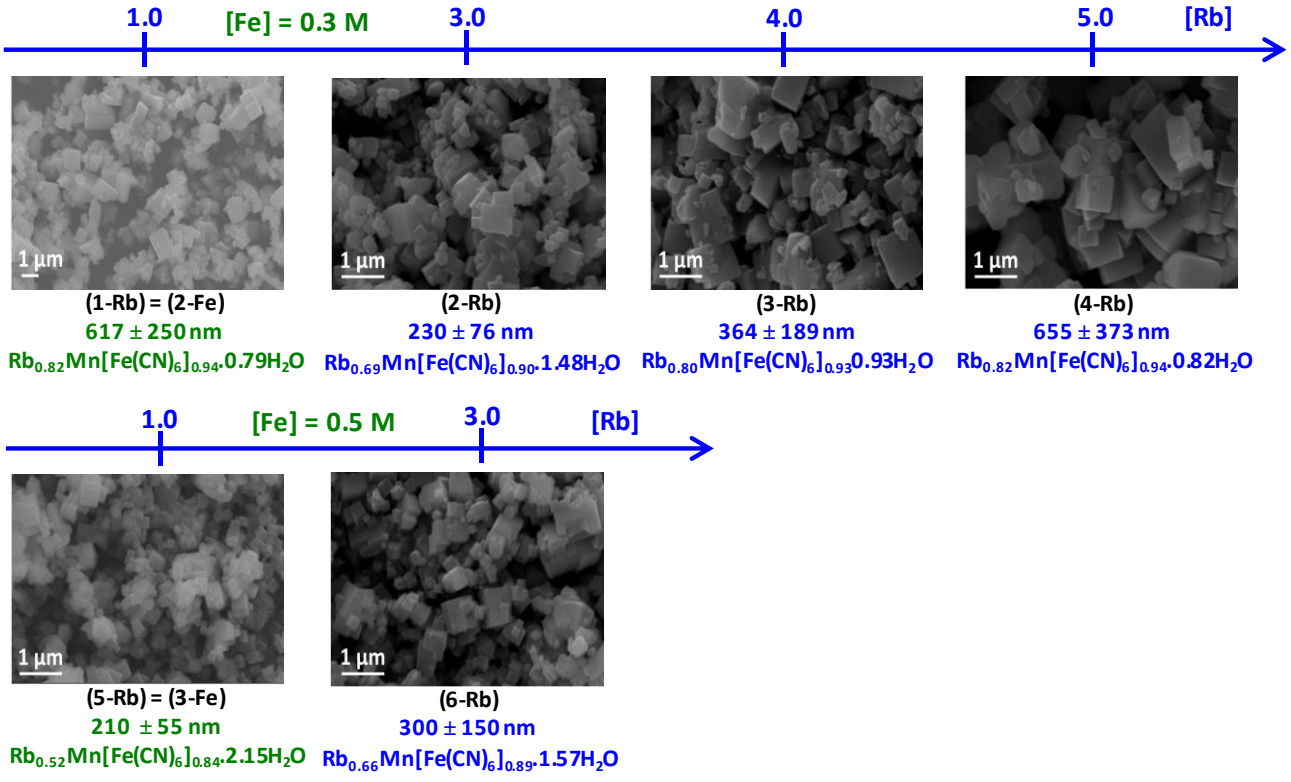

Figure 5: Chart showing the impact of [RbCl] on the composition and size with the corresponding SEM images of each compound.

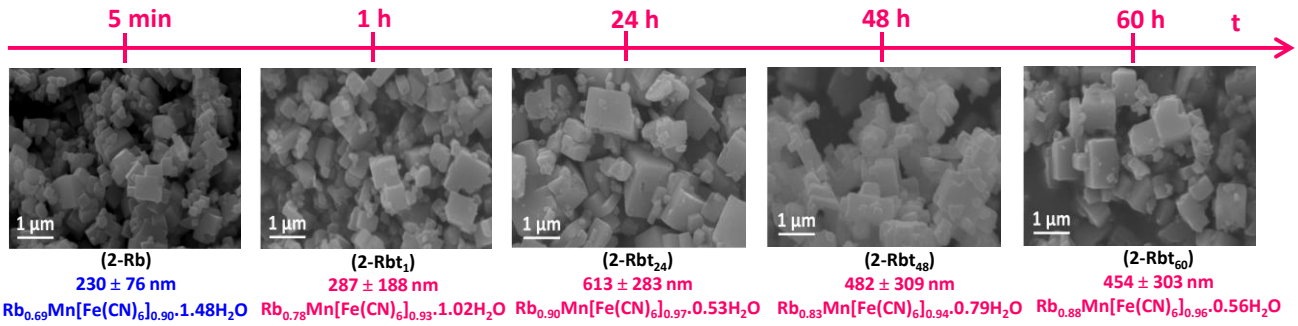

Figure 6: Chart showing the impact of stirring time on the composition and size with the corresponding SEM images of each compound.

when the [RbCl] increased from 3.0 M to 5.0 M, the size increased 3 times from 230 nm to 655 nm. Noticeably, the only decrease in the size occurred when [RbCl] increase from 1.0 M to 3.0 M with [Fe] = 0.3 M. The general trend probably originates from an increase of the ionic strength when the [RbCl] increases, giving rise to the screening of the negative charges at the surface of the particle. Then, the particles aggregate to form bigger ones. The coherent domain sizes obtained from PXRD support this hypothesis. As the [RbCl] increases, the coherent domain size remains stable, in the range of 131 – 161 nm. It may indicate that the particles do not grow anymore, at least crystallographically (Table S6). The observation of big particles in SEM might come from their aggregation.

Regarding the composition, the impact of rubidium concentration in the solution seems modest on its final amount. Indeed, the Rb^{I} content remains almost constant along the series with $Rb_{0.82}$ **(1-Rb = 2-Fe)**, $Rb_{0.69}$ **(2-Rb)**, $Rb_{0.80}$ **(3-Rb)** and $Rb_{0.82}$ **(4-Rb)** when the iron precursor concentration is 0.3 M and slightly increases from $Rb_{0.52}$ **(5-Rb = 3-Fe)** to $Rb_{0.66}$ **(6-Rb)** when the iron precursor concentration is 0.5 M.

The impact of the initial [RbCl] on the Rb^{I} content is modest, with a small increase as the initial concentration rises. Another way to enhance the Rb^{I} content is to let more time to this cation to diffuse inside the structure. Therefore, the effect of stirring time was further analyzed.

The effect of stirring time

The effect of stirring time was studied starting from the reactant concentrations that afford the smallest particles (231 nm) with the highest Rb^{I} content **(**0.69**, 2-Rb)**. Figure 6 reports the SEM images, the size and composition of the RbMnFe particles obtained by increasing the stirring time after addition. The cubic particles have sizes of 230 ± 76 nm **(**5 min, **2-Rb)**, 287 ± 188 nm **(**1 h, **2-Rbt$_1$)**, 613 ± 283 nm **(**24 h, **2-Rbt$_{24}$)**, 482 ± 309 nm **(**48 h, **2-Rbt$_{48}$)**, 454 ± 303 nm **(**60 h, **2-Rbt$_{60}$)**. From 5 min to 24 h of stirring the size increases from 230 nm to 613 nm. Upon further stirring, the size decreases down to 454 nm for 60 h. Most probably, the nucleation process dominates until 5 min after mixing the precursors. After that, the insertion of Rb ion in the structure accompanied with the aggregation process mainly took place, leading to the formation of bigger particles with higher Rb composition. This mechanism is supported by the obtained coherent domain size from PXRD (Table S6), as the stirring time increases from 5 min to 60 h, the coherent domain size stays steadily in the range 131 – 157 nm. The particles do not grow, but aggregate to form bigger particles. Moreover, the Rb insertion process is favored during the stirring time, resulting in the decrease of the surface charge which induces the coalescence of the particles.

Regarding the composition, it evolves along the series as $Rb_{0.69}$ **(2-Rb)**, $Rb_{0.78}$ **(2-Rbt$_1$)**, $Rb_{0.90}$ **(2-Rbt$_{24}$)**, $Rb_{0.83}$ **(2-Rbt$_{48}$)** and $Rb_{0.88}$ **(2-Rbt$_{60}$)**. From 5 min to 24 h under stirring, the Rb^{I} content increases from 0.69 to 0.9. Upon further stirring, it remains rather stable down to 0.88 for 60 h of stirring.

The noticeable tendency is that the bigger the particles, the higher the Rb composition in the structure.

Switching properties

The switching properties were recorded following the thermal evolution of molar magnetic susceptibility (χ_M) times the temperature. This family of compounds being easily thermally quenched in a metastable state at low temperature[32,33] this quenching effect was specifically measured by quickly introducing the sample at 10 K in the magnetometer and increase the temperature at 0.5 K min^{-1}. Figure 7 reports the thermal dependence of the $\chi_M T$ value of compound **(1-Fe)** as a typical example, all the other measurements are collected in supplementary data (Figure S6).

The red curve corresponds to the measurement of the quenched sample leading to the determination of the Thermally-Induced Excited Spin-State Trapping limit temperature[26] (T(TIESST)) that shows the relaxation temperature of the thermally-quenched HT* phase upon heating at 0.5 K min^{-1}. Below 110 K, its behavior clearly shows the differences in the magnetic exchange interactions between the ferromagnetic LT and the antiferromagnetic HT* phases[34]. Above 110 K, this thermally-quenched metastable HT* state relaxes to the stable LT phase. The T(TIESST) temperature is determined from the minimum of the derivative of this curve and found to be at 123 K in this example.

From 350 to 225 K, in the cooling mode, the $\chi_M T$ value slightly decreases before experiencing a drastic decrease down to 150 K, from 4.6 cm^3 K mol^{-1} to 3.17 cm^3 K mol^{-1}. Below 150 K, the $\chi_M T$ value increases as a consequence of the ferromagnetic exchange present between the manganese ions[11,35]. Upon warming the $\chi_M T$ value increases again drastically from 260 to 320 K, drawing a hysteresis loop of 78 K large, between $T_{1/2}\downarrow$ = 208 K and $T_{1/2}\uparrow$ = 286 K ($T_{1/2}$ being the temperature at which half of

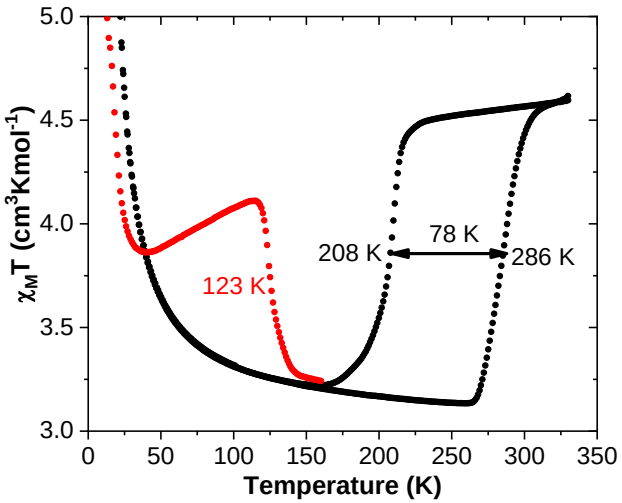

Figure 7: Thermal dependence of the $\chi_M T$ product of the compound **(1-Fe)**, recorded at 0.5 K min^{-1} under 5 000 Oe of applied magnetic field. The red points are related to the TIESST measurement and the black dots to the second thermal cycle.

the compound has switched). This experiment has been performed for all the samples and the data are collected in Table 1. Over all the samples, hysteresis width ranging from 71 K to 110 K were observed. The switching temperatures in the cooling mode are ranging from 181 K to 235 K and that in the warming mode from 286 K to 306 K. When the Rb content is lower than 0.7, the transition becomes gradual and the variation in $\chi_M T$ values between the LT and HT phases is getting smaller. Especially, when Rb content is 0.52 **(3-Fe)**, the shape of the hysteresis is distorted, with few amount of switching leading to difficult determination of the switching temperatures.

Discussion

The control over the size and composition of the RbMnFe compounds is possible through simple chemical tuning. The size is significantly reduced when the concentration of $K_3[Fe(CN)_6]$ increases. On the contrary, the size increases when the stirring time or the concentration of RbCl increases. Our observation of the size evolution is in line with previous works[9] showing that when Prussian Blue Analogs nanoparticles are synthesized with an excess of $K_3[Fe(CN)_6]$, small nanoparticles are stabilized because $K_3[Fe(CN)_6]$ provides an excess of negative charges on the surface of nanoparticles, preventing them from aggregation and so from growing. Similarly, when the RbCl salt concentration increases, the ionic strength increases leading to bigger particles.

Looking at the Rb^I composition in more detail, it increases when the concentration of RbCl or the stirring time is enlarged. However, the Rb content goes down when the concentration of $K_3[Fe(CN)_6]$ increases. While the particles are growing in size, the Rb^I content increases (Figure 8). This is a general trend we can extract from the whole study, leading to antagonistic effects: getting small nanoparticles with high rubidium content looks contradictory. In the following relationship the bigger the size the higher the Rb composition, a balance of those parameters should be found in order to obtain small particles exhibiting switching properties. To go beyond this first study, the size and composition can be also tuned by other parameters, such as the temperature, the addition rate, the volume of the precursors, etc. This will be the purpose of another study.

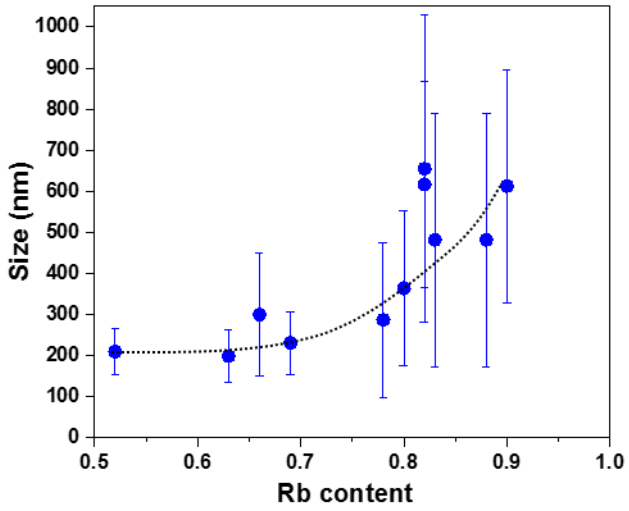

Figure 8: Particle size as function of the Rb^I content. The dotted line is a guide for the eyes.

From the previous studies, it has been shown that the switching properties depend on the Rb^I composition[12,21,33]: the higher the Rb^I content, the higher the switching temperatures, the narrower the hysteresis. Figure 9a reports the evolution the switching temperatures as function of the Rb^I content for the 12 compounds synthesized here and compared with data from the literature reported on microscopic particles. This figure clearly shows that $T_{1/2}\downarrow$ is more affected by the Rb^I content than $T_{1/2}\uparrow$. This leads to a global widening of the hysteresis loop while the Rb^I content decreases. This agrees with the previous observation made on microparticles (grey dots on Figure 9a). The observation of a small hysteresis for $Rb_{0.52}$ (compound **3-Fe**) might come from some inhomogeneity in composition. Indeed, the variation of $\chi_M T$ value upon switching is smaller than for all the other compounds, indicating that only a small amount of the sample switches. However, since the nanoparticles are bigger than 200 nm, the contribution of surface inhomogeneities is small. Indeed, if we consider an outer-shell of 5 nm with a strongly different composition than in the core, it only represents 7 % of the whole volume of the particle. Then, inhomogeneities might come from the presence of a size distribution inside the sample, correlated to a composition gradient. In the case of $Rb_{0.52}$ the size distribution is small (210 ± 55 nm), limiting the impact of such effect on the composition. The impact of size reduction on the switching properties seems to allow observing the switching behavior at lower rubidium content compared to the microparticle studies, as seen from the crossing of T(TIESST) with the thermal hysteresis. The "phase diagram" in Figure S8 reports the evolution of the switching temperatures, including T(TIESST) as function of the composition. As for the previous study made on microparticles[33], as the hysteresis is shifted towards low temperatures, the T(TIESST) slightly increases. If one considers the linear fit of each set of points, a crossing between T(TIESST) and $T_{1/2}\downarrow$ occurs around x = 0.5. Above this value, the switching property is expected to be observed while below this value the compound should remain in

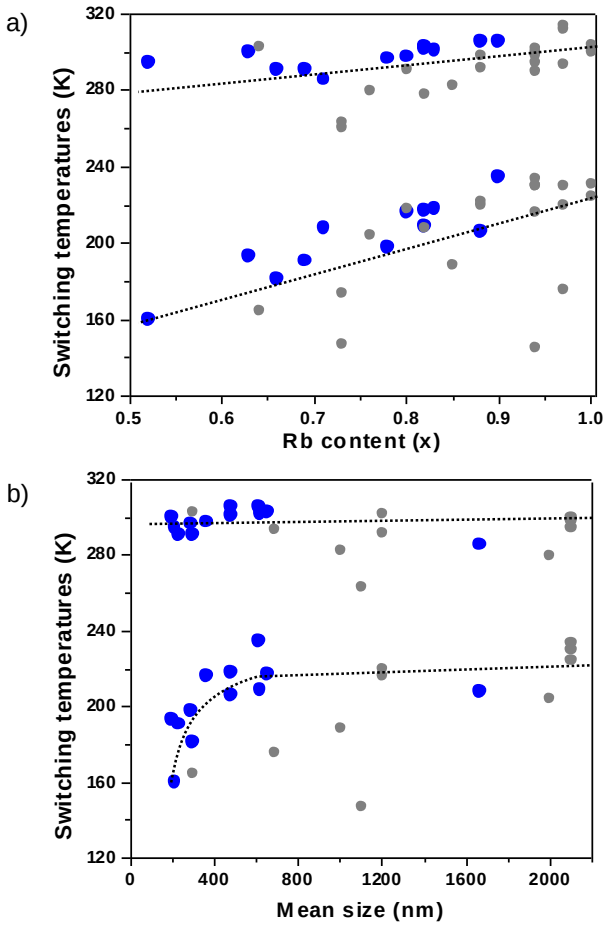

Figure 9: Switching temperatures $T_{1/2}\downarrow$ and $T_{1/2}\uparrow$ as function of the Rb^{I} content (a) and particles size (b). The blue dots correspond to the particles obtained during the present study and the grey points relate to the literature data. The grey dotted lines are guides for the eyes.

the HT phase[33]. This agrees well with our observation on the nanoparticles for which below x = 0.52, the switching properties are suppressed.

Figure 9b reports the evolution of the switching temperatures as function of the particles size. It shows a moderate impact of the size reduction on the switching properties with data that do not strongly deviate from the previous ones obtained on microparticles. This is probably due to the fact that, with our chemical approach the nanoparticles remain quite "large" (above 200 nm) preventing size and surface effect to be visible. However, below 400 nm, one may suspect a deviation of $T_{1/2}\downarrow$ to the linear trend observed for higher sizes. Indeed, while below 400 nm $T_{1/2}\uparrow$ remains constant, $T_{1/2}\downarrow$ seems to exhibit an additional decrease upon size reduction. Since there is no linear correlation between the size and the composition, one should not expect a linear $T_{1/2}$ = f(size) relationship. This 400 nm size corresponds well to the change of slope in Figure 8 that correlates the size and the composition. The size reduction might affect more the cubic to tetragonal phase transition than the reverse one. Moreover, this kind of behavior as already been observed while studying the size reduction of spin crossover materials[36].

Conclusion

In this paper, we targeted the rational design of switchable nanoparticles of the $Rb_xMn[Fe(CN)_6]_{(2+x)/3}.nH_2O$ compound. We succeeded to reduce the size of the compound to 200 nm with the preservation of switching properties near room temperature. This study shows 1) the special care to bring to the determination of the chemical composition using several techniques; 2) that the obtaining of switchable nanoparticles of this RbMnFe compound results from an antagonistic effect: the smaller the particles, the smaller the Rb^{I} content. Since the switching temperatures and the hysteresis width depend on the Rb^{I} content, this latter aspect is crucial.

ASSOCIATED CONTENT

Supporting Information. A literature survey as well as the extensive characterizations of the synthesized compounds can be found in Supplementary information in addition to other relevant characterizations of all the compounds.

AUTHOR INFORMATION

Corresponding Author

* guillaume.chastanet@icmcb.cnrs.fr
* nathalie.daro@icmcb.cnrs.fr

Author Contributions

The manuscript was written through contributions of all authors. / All authors have given approval to the final version of the manuscript.

Funding Sources

ANR HEROES (ANR-17-CE09-0010-01)

ACKNOWLEDGMENT

CNRS, ANR project (HEROES ANR-17-CE09-0010-01) for the funding. The XRD measurements are performed by Eric Lebraud at the XRD center of ICMCB. Patrick Rosa, Baptiste Vignolle, Laetitia Etienne for elemental analysis training. Sonia Buffiere for SEM training.

REFERENCES

[1] Nemat-Nasser, S.; Nemat-Nasser, S.; Plaisted, T.; Starr, A.; Vakil Amirkhizi, A. in Biomimetics: biologically inspired technologies, *CRC Press*, **2005**, 309.

[2] Létard, J.-F.; Chastanet, G.; Guionneau, P.; Desplanches C. in Spin-crossover materials - properties and applications, Ed. M.A. Halcrow, *John Wiley & Sons, Chichester, UK*, **2012**, 475.

[3] Bertoni, R.; Cammarata, M.; Lorenc, M.; Matar, S.; Létard, J.-F.; Lemke, H.; Collet, E. Ultrafast light-induced spin-state trapping photophysics investigated in Fe(phen)2(NCS)2 spin-crossover crystal. *Acc. Chem. Res.* **2015**, *48*, 774–781.

[4] a) Freysz, E.; Montant, S.; Létard, S.; Létard, J.-F. Single laser pulse induces spin state transition within the hysteresis loop of an Iron compound. *Chem. Phys. Lett*. **2004**, *394*, 318–323; b) Bonhommeau, S.; Molnar, G.; Galet, A.; Zwick, A.; Real, J.A.; McGarvey, J.J.; Bousseksou, A. One shot laser pulse induced reversible spin transition in the spin-crossover complex $[Fe(C_4H_4N_2)\{Pt(CN)_4\}]$ at room temperature. *Angew. Chem. Int. Ed*. **2005**, *44*, 4069–4073.

[5] a) Hellel, W.; Ould Hamouda, A.; Degert, J.; Létard, J.-F.; Freysz, E. Switching of spin-state complexes induced by the interaction of a laser beam with their host matrix. *Appl. Phys. Lett.* **2013**, *103*, 143304; b) Freysz, E.; Létard, J.-F. Procede et dispositif de visualisation d'un rayonnement electromagnetique tetrahertz. Patents FR **2014**/2993978, WO **2014**/2014016525.

[6] a) Gallé, G.; Etrillard, C.; Degert, J.; Guillaume, F.; Létard, J.-F.; Freysz, E. Study of the fast photoswitching of spin crossover nanoparticles outside and inside their thermal hysteresis loop. *Appl. Phys. Lett.* **2013**, *102*, 063302; b) Hu, Y.; Picher, M.; Tran, N.M.; Palluel, M.; Stoleriu, L.; Daro, N.; Mornet, S.; Enachescu, C.; Freysz, E.; Banhart, F.; Chastanet, G. Photo-thermal switching of individual plasmonically activated spin crossover nanoparticle imaged by ultrafast transmission electron microscopy. *Adv. Mater.* **2021**, 2105586.

[7] a) Palluel, M.; Tran, N.M.; Daro, N.; Buffière, S.; Mornet, S.; Freysz, E.; Chastanet, G. The interplay between surface plasmon resonance and switching properties in gold@spin crossover nano-composites. *Adv. Func. Mater.* **2020**, *30*, 2000447; b) Tran, N.M.; Palluel, M.; Daro, N.; Chastanet, G.; Freysz, E. Time-resolved study of the photoswitching of gold nanorods coated with a spin-crossover compound shell. *J. Phys. Chem. C.* **2021**, *125*, 22611–22621.

[8] a) Piernas Munoz, M.J.; Castillo Martinez, E. Prussian blue based batteries, *Springer* **2018**; b) Assis, L.M.N.; Leones, R.; Kanichi, J.; Pawlicka, A.; Silva, M.M. Prussian blue for electrochromic devices. *J. Electro. Chem*. **2016**, *777*, 33–39; c) Ferlay, S.; Mallah, T.; Ouahès, R.; Veillet, P.; Verdaguer, M. A room-temperature organometallic magnet based on Prussian blue. *Nature* **1995**, *378*, 701–703.

[9] Catala, L.; Mallah, T. Nanoparticles of Prussian blue analogs and related coordination polymers: From information storage to biomedical applications. *Coord. Chem. Rev*. **2017**, *346*, 32–61.

[10] Tokoro, H.; Ohkoshi, S. in Progress in nano-electro-optics VII, *Springer*, **2010**, 1.

[11] Ohkoshi, S.; Tokoro, H.; Utsunomiya, M.; Mizuno, M.; Abe, M.; Hashimoto, K. Observation of spin transition in an octahedrally coordinated manganese(II) compound. *J. Phys. Chem. B*, **2002**, 106, 2423–2425.

[12] Ohkoshi, S.; Matsuda, T.; Tokoro, H.; Hashimoto, K. A surprisingly large thermal hysteresis loop in a reversible phase transition of $Rb_xMn[Fe(CN)_6]_{(x+2)/}3.zH_2O$. *Chem. Mater.* **2005**, *17*, 81–84.

[13] Ohkoshi, S.; Saito, S.; Matsuda, T.; Nuida, T.; Tokoro, H. Continuous change of second-order nonlinear optical activity in a cyano-bridged coordination polymer. *J. Phys. Chem. C* **2008**, *112*, 13095–13098.

[14] a) Ould-Hamouda, A.; Iazzolino, A.; Tokoro, H.; Ohkoshi, S.; Freysz, E. Second-harmonic and terahertz generation in a Prussian-blue analogue. *Eur. J. Inorg. Chem*. **2018**, 378–384; b) Ould-Hamouda, A.; Iazzolino, A.; Tokoro, H.; Ohkoshi, S.; Freysz, E. Large optical third-order nonlinearities in a switchable Prussian blue analogue. *Opt. Mater. Express* **2017**, *7*, 444–453.

[15] Nuida, T.; Matsuda, T.; Tokoro, H.; Sakurai, S.; Hashimoto, K.; Ohkoshi, S. Nonlinear magnetooptical effects caused by piezoelectric ferromagnetism in F43m-type Prussian blue analogues. *J. Am. Chem. Soc*. **2005**, *127*, 11604–11605.

[16] Tokoro, H.; Nakagawa, K.; Imoto, K.; Hakoe, F.; Ohkoshi, S. Zero thermal expansion fluid and oriented film based on a bistable metal-cyanide polymer. *Chem. Mater*., **2012**, *24*, 1324–1330.

[17] Tokoro, H.; Shiro, M.; Hashimoto, K.; Ohkoshi, S. Single crystal of a Prussian blue analog based on rubidium manganese hexacyanoferrate. *Z. Anorg. Allg. Chem.* **2007**, *633*, 1134–1136

[18] Osawa, H.; Iwazumi, T.; Tokoro, H.; Ohkoshi, S.; Hashimoto, K.; Shoji, H.; Hirai, E.; Nakamura, T.; Nanao, S.; Isozumi, Y. Thermal phase transition of $RbMnFe(CN)_6$ observed by X-ray emission and absorption spectroscopy. *Solid State Commun.* **2003**, *125*, 237–241.

[19] Yokoyama, T.; Tokoro, H.; Ohkoshi, S.; Hashimoto, K.; Okamoto, K.; Ohta, T. Photoinduced phase transition of $RbMnFe(CN)_6$ studied by x-ray-absorption fine structure spectroscopy. *Phys. Rev. B*, **2002**, *66*, 184111.

[20] Kato, K.; Moritomo, Y.; Takata, M.; Sakata, M.; Umekawa, M.; Hamada, N.; Ohkoshi, S.; Tokoro, H.; Hashimoto, K. Direct observation of charge transfer in double-perovskite-like $RbMn[Fe(CN)_6]$. *Phys. Rev. Lett.* **2003**, *91*, 255502.

[21] Asahara, A.; Nakajima, M.; Fukaya, R.; Tokoro, H.; Ohkoshi, S.; Suemoto, T. Ultrafast dynamics of reversible photoinduced phase transitions in rubidium manganese hexacyanoferrate investigated by midinfrared CN vibration spectroscopy. *Phys. Rev. B*, **2012**, *86*, 195138.

[22] Tokoro, H.; Miyashita, S.; Hashimoto, K.; Ohkoshi, S. Huge thermal hysteresis loop and a hidden stable phase in a charge-transfer phase transition of $Rb_{0.64}Mn[Fe(CN)_6]_{0.88}\cdot 1.7H_2O$. *Phys. Rev.B*, **2006**, *73*, 172415.

[23] Risset, O.N.; Knowles, E.S.; Ma, S.; Meisel, M. W.; Talham, D.R. $Rb_jM_k[Fe(CN)_6]_l$ (M = Co, Ni) Prussian blue analogue hollow nanocubes: A new example of a multilevel pore system. *Chem. Mater*. **2013**, *25*, 42–47

[24] Harvey, D. Analytical chemistry 2.0. Standardizing analytical methods. http://chem.libretexts.org/link?5726

[25] Bergmann, R.B.; Bill, A. On the origin of logarithmic-normal distributions: An analytical derivation, and its application to nucleation and growth processes. *J. Crystal Growth*, **2008**, *110*, 3135–3138

[26] Chastanet, G.; Desplanches, C.; Baldé, C.; Rosa, P.; Marchivie, M.; Guionneau, P. A critical review of the T(LIESST) temperature in spin crossover materials – what it is and what it is not. *Chem. Sq.* **2018**, *2*

[27] Vertelman, E. J. M.; Maccallini, E.; Gournis, D.; Rudolf, P.; Bakas, T.; Luzon, J.; Broer, R.; Pugzlys, A.; Lummen, T. T. A.; Loosdrecht, P. H. M.; Koningsbruggen, P. The influence of defects on the electron-transfer and magnetic properties of $Rb_xMn[Fe(CN)_6]_y\cdot zH_2O$. *Chem. Mater*. **2006**, *18*, 1951–1963.

[28] Ohkoshi, S.; Tokoro, H.; Hashimoto, K. Temperature- and photo-induced phase transition in rubidium manganese hexacyanoferrate. *Coord. Chem. Rev*. **2005**, *249*, 1830–1840.

[29] Petricek, V.; Dusek, M.; Palatinus, L. Crystallographic computing system JANA2006: general features. *Z. Kristallogr.* **2014**, *229***,** 345–352

[30] Tokoro, H.; Ohkoshi, S.; Hashimoto, K. One-shot-laser-pulse-induced demagnetization in rubidium manganese hexacyanoferrate. *Appl. Phys. Lett.* **2003**, *82*, 1245–1247.

[31] Tokoro, H.; Ohkoshi, S.; Matsuda, T.; Hashimoto, K. A large thermal hysteresis loop produced by a charge-transfer phase transition in a rubidium manganese hexacyanoferrate. *Inorg. Chem.* **2004**, *43*, 5231–5236.

[32] Tokoro, H.; Matsuda, T.; Miyashita, S.; Hashimoto, K.; Ohkoshi, S. Crystal structures of photo-induced phase and rapidly-cooled phase in $Rb_{0.73}Mn[Fe(CN)_6]_{0.91}\cdot 1.4H_2O$ Prussian blue analog. *J. Phys. Soc. Jpn*. **2006,** *75*, 085004.

[33] Létard, J. F.; Chastanet, G.; Tokoro, H.; Ohkoshi, S. Rubidium manganese hexacyanoferrate solid solutions: Towards hidden phases. *Curr. Inorg. Chem.* **2016**, *6*, 34–39.

[34] Tokoro, H.; Matsuda, T.; Nuida, T.; Moritomo, Y. ; Ohoyama, K. ; Loutete Dangui E. D. ; Boukheddaden, K. ; Ohkoshi, S.-I. Visible light-induced reversible photomagnetism in rubidium manganese hexacyanoferrate. *Chem. Mater.*, **2008**, *20*, 423

[35] Tokoro, H.; Hashimoto, K.; Ohkoshi, S. Photo-induced charge-transfer phase transition of rubidium manganese hexacyanoferrate in ferromagnetic and paramagnetic states. *J. Mag. Mag. Mater*. **2007**, *310*, 1422–1428.

[36] a) Oubouchou, H.; Slimani, A.; Boukheddaden, K. Interplay between elastic interactions in a core-shell model for spin-crossover nanoparticles. *Phys. Rev. B.*, **2013**, *87*, 104104; b) Etrillard, C. Synthèse de nanoparticules à transition de spin et étude des propriétés,

application en électronique moléculaire. *PhD doctorate, Univ. Bordeaux*, **2011**.